Research Article Vol. 31, No. 14 / 3 Jul 2023 / Optics Express 23245
Optics EXPRESS

Single-shot detection of bacterial spores with Yb-laser-based CARS spectroscopy

NICOLA COLUCCELLI,[1,2,*] GIOVANNI CICHELLI,[1] PAOLO LAPORTA,[1,2] AND GIULIO CERULLO[1,2]

[1]Dipartimento di Fisica - Politecnico di Milano, Piazza Leonardo da Vinci 32, 20133 Milano, Italy
[2]Istituto di Fotonica e Nanotecnologie - CNR, Piazza Leonardo da Vinci 32, 20133 Milano, Italy
[*]nicola.coluccelli@polimi.it

Abstract: We present a system based on a high-energy femtosecond ytterbium laser seeding an optical parametric amplifier and a photonic crystal hollow core fiber (PCHCF) compressor for coherent anti-Stokes Raman scattering (CARS) spectroscopy. The PCHCF provides spectral broadening of the Stokes pulse which is then compressed to a duration matched to that of the pump pulse. In these conditions, the excitation efficiency of vibrational levels in the target molecules is largely improved, as the time gating effect due to the mismatch between the durations of the pump and Stokes pulses is avoided. Experiments are presented along with a theoretical model to quantify expected improvement of sensitivity. The system is used to detect bacterial spores deposited on a surface with a single laser shot at unprecedented signal-to-noise ratio.

1. Introduction

Coherent Anti-Stokes Raman Scattering (CARS) is a third-order nonlinear optical process which is a powerful spectroscopic tool to study the vibrational properties of molecules. In CARS two ultrashort and frequency-detuned light pulses, the pump and the Stokes, drive a vibrational coherence in the sample, which is then read by an interaction with a probe pulse (often the pump pulse itself), generating a blue-shifted signal at the anti-Stokes frequency. CARS has been extensively applied in a variety of fields such as chemistry, physics, and biology, providing valuable information about molecular structure and dynamics [1,2]. The main advantage of CARS spectroscopy over traditional spontaneous Raman (SR) is the dramatic increase of signal, due to the coherent superposition of vibrational responses from the excited molecular oscillators, in contrast to SR, where the superposition is incoherent [3–5]. As a result, the CARS signal increases quadratically with the number of molecular oscillators whereas SR signal increases linearly; this is a great advantage in application where the concentration of target molecules is high, however, it becomes a limit at low concentration. The coherent addition also results in a highly directional output, which greatly facilitates the signal collection. The large CARS signal allows for high-speed vibrational imaging, which is not possible with SR microscopy [4,6,7]. The major drawback of CARS is the so-called non-resonant background (NRB), a signal arising from the electronic contribution to the third-order susceptibility $\chi^{(3)}$, which is often much stronger than the resonant vibrational signal, ultimately limiting the sensitivity of CARS for detection of weak Raman bands.

In recent years, there have been significant advances in CARS spectroscopy, including the development of new instrumentation and techniques based on femtosecond lasers, which allow for efficient excitation of vibrational modes of molecules through their high-intensity, ultra-short light pulses [8–10]. CARS microscopy finds several applications in biology, where it has been used to explore the molecular composition of a range of biological systems such as individual cells, tissues and organs, allowing one to identify in a label-free way proteins, lipids, and nucleic acids. CARS can also be used for remote sensing applications such as gas thermometry [11,12], or detection of explosives and chemicals even in standoff mode [13–18]. In this context, a

#493869 https://doi.org/10.1364/OE.493869
Journal © 2023 Received 21 Apr 2023; revised 8 Jun 2023; accepted 12 Jun 2023; published 27 Jun 2023

Optics EXPRESS

variation of CARS, known as hybrid fs/ps CARS (hybrid-CARS) [11,19] has culminated in the successful demonstration of bacterial spores detection [20–22]. Hybrid-CARS uses a couple of femtosecond pump/Stokes pulses to impulsively excite a molecular coherence, and then a suitably delayed picosecond probe pulse to read the coherence, generating the anti-Stokes signal. As the NRB originates from a four-wave-mixing process involving virtual states, it requires temporal overlap between the pump, Stokes and probe pulses, and can be greatly reduced by delaying the probe pulse; on the other hand, the molecular coherence, which has typical decay times of a few picoseconds, can still be sampled at relatively intense levels. The peculiarity of the hybrid-CARS reported in [20–22] with respect to other time-delayed CARS techniques is that the pump/Stokes pulses are placed in the temporal node of a sinc-shaped probe pulse in order to virtually suppress all of the NRB, therefore maximizing the sensitivity.

Until recently, hybrid-CARS systems were based on Ti:sapphire technology, which due to its complexity could be operated only within well-controlled laboratory environments and required large setups. To overcome this limitation, we have developed setups based on the technology of femtosecond Yb-lasers [23,24], featuring industrial grade stability performance along with a reduced complexity and footprint, which open the path to in-field applications. Using our Yb-based system, we demonstrated detection of *Bacillus atrophaeus* (*B. atrophaeus*) bacterial spores at a standoff distance of 1 m, with an integration time of 1 s, through the Raman fingerprint of the molecule calcium dipicolinate (CaDPA), which is characteristic of spores [22]. However, the performance of the system were limited by the mismatch between the durations of the pump (30-fs) and Stokes (250-fs) pulses used for excitation of the vibrational coherence, resulting in a time-gating effect where a considerable amount of the pulse energy was not used.

In this paper, we present an extended version of our setup based on the adoption of a gas-filled hollow-core photonic crystal fiber (HCPCF) to reduce the duration of the Stokes pulse to 48 fs through spectral broadening and post-compression, ultimately avoiding the time gating effect caused by the much shorter pump pulse. We present a theoretical model to quantify the gain of line intensity in a measured CARS spectrum attainable with matched pump/Stokes pulse durations, along with experimental measurements to support the model. We show how the extension of our earlier experimental work [22] yields identification of a small sample of *B. atrophaeus* spores deposited on a surface at a distance of 20 cm from the system using a single laser shot. The reported signal to noise ratio (SNR) and overall spectral quality are superior to any previous stand-off measurement based on CARS spectroscopy.

2. Theoretical model

The description of hybrid-CARS spectroscopy in the time domain is based on two femtosecond pump/Stokes pulses used to generate a molecular coherence and a suitably delayed picosecond probe pulse to read the coherence; in addition, the probe is shaped to a sinc temporal profile and the pump/Stokes pulses are placed in its node to avoid the generation of NRB. In the frequency domain, the convolution between the broadband spectra of the two excitation pulses determines the range of Raman frequencies which can be observed, the frequency resolution being set by the bandwidth of the probe. The concept behind this paper is that the SNR and overall quality of spectra observed by hybrid-CARS spectroscopy are largely dependent upon matching the durations of the two pump/Stokes excitation pulses. The concept is illustrated in Fig. 1. In case of a large mismatch between the durations of the excitation pulses, the longer one is effectively time gated by the shorter, and a large amount of its energy content is not even used to excite the molecular vibration. The overall bandwidth of the CARS spectrum resulting from this condition is substantially reduced as well as the SNR of the Raman lines, especially those on the tails of the excitation profile. On the other hand, in case of a close match between the durations of the pump/Stokes pulses, the energies of both pulses are effectively used, resulting in optimized excitation; the bandwidth is also improved.

Optics EXPRESS

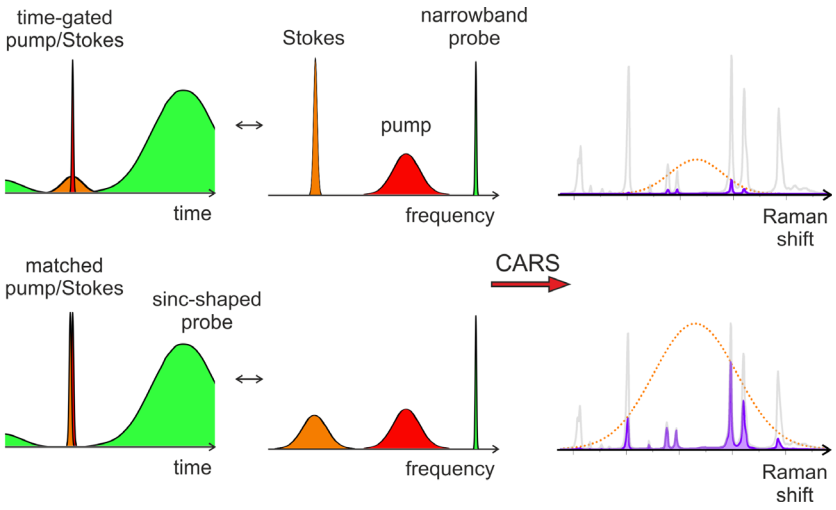

Fig. 1. The concept of hybrid-CARS spectroscopy discussed in this paper. Two different configurations of the pump and Stokes pulses are considered: on top, the Stokes pulse is time-gated by the much shorter pump pulse, resulting in low-efficiency and narrow-band excitation of Raman vibrations; on bottom, the durations of the pump and Stokes pulses are matched, leading to dramatic improvement of visibility, bandwidth, and hence, overall quality of the resulting CARS spectrum. The picture shows the spontaneous Raman spectra of a reference target substance (NaDPA, gray line), the excitation profiles due to the pump/Stokes pulses (orange dotted line), and the corresponding CARS spectra (violet line).

The theoretical model that follows is built upon the general theory of CARS presented by Silberberg et al. [10], later adapted to hybrid-CARS by Scully et al. [21]. More specifically, in this latter work, the focus has been put on the dependence of the CARS signal onto the bandwidth and delay of the probe pulse, for the purpose of optimizing measurement parameters for bacterial spores detection. For the same purpose, here, we focus on the modeling of the CARS signal as a function of the duration of the Stokes pulse with respect to the pump (or viceversa), to quantify the gain in terms of SNR which results from matching the duration of the two excitation pulses. The interaction can be explained in terms of the third order nonlinear polarization $P^{(3)}(\omega)$ oscillating at an optical frequency ω, with the usual resonant and non-resonant contributions expanded as follows:

$$P^{(3)}(\omega) = P_R^{(3)}(\omega,\tau) + P_{NR}^{(3)}(\omega,\tau) = \int_0^{+\infty} \left[\chi_R^{(3)}(\Omega) + \chi_{NR}^{(3)}\right] E_3(\omega-\Omega,\tau) S_{12}(\Omega) d\Omega \qquad (1)$$

where $\chi_R^{(3)}(\Omega)$ and $\chi_{NR}^{(3)}$ are the third order resonant and non-resonant susceptibility, respectively, Ω is the Raman frequency shift, $S_{12}(\Omega) = \int_0^{+\infty} E_1(\omega'+\Omega)E_2^*(\omega')d\omega'$ is the excitation profile given by the cross-correlation of the pump and Stokes spectral amplitudes, $E_1(\omega)$ and $E_2(\omega)$, respectively, and $E_3(\omega,\tau)$ is the probe spectral amplitude with explicit dependence on the delay τ with respect to the pump/Stokes pulses. The resonant part $\chi_R^{(3)}$ of the third order nonlinear susceptibility is expressed as the superposition of complex Lorentzian responses corresponding to the different vibrational transitions of the probed molecules

$$\chi_R^{(3)}(\Omega) = \sum_j \frac{N_j \sigma_j}{\Omega - \Omega_j - i\Gamma_j} \qquad (2)$$

Optics EXPRESS

where N_j is the concentration of Raman active molecules, σ_j are the cross sections, Ω_j are the resonance Raman frequencies, and Γ_j are the linewidths of the vibrational transitions. The non-resonant part $\chi^{(3)}_{NR}$, associated to both the targeted molecules and the surrounding medium, can be assumed real and frequency independent, and gives rise to the NRB.

For the analysis that follows, the spectral profiles of the broadband pump and Stokes pulses are assumed Gaussian with center frequency ω_1, ω_2, and FWHM bandwidth $\Delta\omega_1$, $\Delta\omega_2$, respectively, whereas the spectrum of the narrowband probe is approximated to a Dirac delta function at a frequency ω_3, and a delay τ with respect to the pump/Stokes:

$$E_i(\omega) = A_i\, e^{-2\,ln2\left(\frac{\omega-\omega_i}{\Delta\omega_i}\right)^2}, \quad i = 1, 2 \tag{3}$$

$$E_3(\omega, \tau) = A_3\, \delta(\omega - \omega_3) e^{i\omega\tau} \tag{4}$$

Note that the energy U_i of the pump/Stokes pulses is given by:

$$U_i = \int_0^{+\infty} |E_i(\omega)|^2\, d\omega = \sqrt{\frac{\pi}{2ln2}}\, |A_i|^2 \Delta\omega_i\,, \quad i = 1, 2 \tag{5}$$

The excitation profile $S_{12}(\omega)$ is then readily calculated, as the convolution of two Gaussian functions is again Gaussian, which yields:

$$S_{12}(\Omega) = S_0\, e^{-2\,ln2\left(\frac{\Omega-\Omega_0}{\Delta\omega_{12}}\right)^2} \tag{6}$$

$$S_0 = \sqrt{\frac{\pi}{2\,ln2}}\, \frac{\Delta\omega_1 \Delta\omega_2}{\Delta\omega_{12}}\, A_1 A_2^* \tag{7}$$

where $\Omega_0 = \omega_1 - \omega_2$ is the center frequency of the excitation profile, and $\Delta\omega_{12} = \sqrt{\Delta\omega_1^2 + \Delta\omega_2^2}$ is the corresponding bandwidth. The spectral intensity of the CARS signal is obtained by the absolute square of Eq. (1) after substitution of Eq. (4):

$$I_{CARS}(\omega) \propto \left|P^{(3)}(\omega)\right|^2 \tag{8}$$

$$= \left| \int_0^{+\infty} \left[\chi^{(3)}_R(\Omega) + \chi^{(3)}_{NR}\right] A_3\, \delta(\omega - \Omega - \omega_3) e^{i(\omega-\Omega)\tau} S_{12}(\Omega) d\Omega \right|^2 \tag{9}$$

$$= \left|\chi^{(3)}_R(\omega - \omega_3) + \chi^{(3)}_{NR}\right|^2 \left|S_{12}(\omega - \omega_3)\right|^2 \left|A_3\right|^2 \tag{10}$$

$$\propto \left[\left|\chi^{(3)}_R(\omega - \omega_3)\right|^2 + \left(\chi^{(3)}_{NR}\right)^2 + 2\chi^{(3)}_{NR}\mathrm{Re}\left\{\chi^{(3)}_R(\omega - \omega_3)\right\}\right] \left|S_{12}(\omega - \omega_3)\right|^2 I_3 \tag{11}$$

which accounts for the well-known, usually detrimental, effect of the NRB to the overall CARS response, ascribed to the frequency-independent term $\left(\chi^{(3)}_{NR}\right)^2$ and to the dispersive interference term $2\chi^{(3)}_{NR}\mathrm{Re}\left\{\chi^{(3)}_R(\omega - \omega_3)\right\}$ that distorts the Lorentzian-shaped vibrational lines. The hybrid-CARS technique provides an effective way to reduce the NRB by placing both pump and Stokes pulses in the zero of the sinc-shaped probe; in this case, the non-resonant response is virtually avoided, and the CARS signal is simply given by:

$$I_{CARS}(\omega) \propto \left|\chi^{(3)}_R(\omega - \omega_3)\right|^2 \left|S_{12}(\omega - \omega_3)\right|^2 I_3 \tag{12}$$

Expression (12) shows how the resonant response $\left|\chi^{(3)}_R\right|^2$ of the target is weighted by the absolute square of the excitation profile $\left|S_{12}\right|^2$, before providing the final CARS signal. This

Optics EXPRESS

happens also in the general case given by Eq. (11), i.e. when the resonant and non-resonant responses are both activated. This clarifies the importance of optimizing the excitation profile for best visibility of the CARS signature of the sample.

The function $\left|S_{12}\right|^2$ can be isolated and measured in samples where vibrational transitions are absent or extremely weak in the range of Raman frequencies excited by the pump/Stokes pulses; in these cases, the resonant part of the third order susceptibility is negligible ($\chi_R^{(3)} \cong 0$), and Eq. (11) reduces to:

$$I_{CARS}(\omega) \propto \left(\chi_{NR}^{(3)}\right)^2 \left|S_{12}(\omega-\omega_3)\right|^2 I_3 \tag{13}$$

showing that a measurement of the CARS signal spectrum provides a scaled replica of the function $\left|S_{12}\right|^2$. This allows for a quantitative analysis of the impact that a mismatch between the pump/Stokes pulse durations, or bandwidths, has on the excitation profile, and ultimately, on the sensitivity of the hybrid-CARS technique. To this purpose, substitution of Eq. (5) into Eqs. (6) and (7) yields:

$$\left|S_{12}(\omega-\omega_3)\right|^2 = U_1 U_2 \left(\frac{\Delta\omega_1 \Delta\omega_2}{\Delta\omega_{12}^2}\right) e^{-4\,ln2\left(\frac{\omega-\omega_3-\Omega_0}{\Delta\omega_{12}}\right)^2} \tag{14}$$

showing an excitation centered at $\omega_3 + \Omega_0$, i.e. the frequency of the probe plus the frequency separation between the pump and Stokes, with a FWHM bandwidth of $\Delta\omega_{12}$. The bandwidth of the Stokes can be expressed as $\Delta\omega_2 = \beta\Delta\omega_1$, where β is a pump/Stokes 'match' parameter that can be tuned from 0 to $+\infty$. While doing this, both the pump and Stokes pulses are compressed to the corresponding transform-limited durations before the CARS interaction takes place, and their energies are kept constant. Interestingly, $\beta \to 0$ or $\beta \to +\infty$ corresponds to a narrowband Stokes or pump, respectively, which leads to conditions where one pulse is time-gated by the other, and only a limited amount of its energy is effectively used (similar to our setup presented in [18,22]); on the other hand, $\beta \cong 1$ corresponds to well matched bandwidths/durations of the pump and Stokes pulses, and hence optimized use of their energy. Equation (14) can be recast into:

$$\left|S_{12}(\omega-\omega_3)\right|^2 = U_1 U_2 \left(\frac{\beta}{1+\beta^2}\right) e^{-4\,ln2\left(\frac{\omega-\omega_3-\Omega_0}{\Delta\omega_1\sqrt{1+\beta^2}}\right)^2} \tag{15}$$

that is a Gaussian profile with an amplitude factor of $\beta/\left(1+\beta^2\right)$ and a FWHM bandwidth of $\Delta\omega_1\sqrt{1+\beta^2}$. Consistently, for a narrowband Stokes with $\beta \to 0$ the bandwidth of the CARS spectral profile reduces to the bandwidth of the pump, $\Delta\omega_1$. The absolute square of the excitation profile $\left|S_{12}(\Omega)\right|^2$ as a function of the Raman shift is plotted in Fig. 2(a) for several values of the β parameter, assuming a pump pulse bandwidth of 330 cm^{-1} and a pump/Stokes detuning of 1290 cm^{-1}, similar to the conditions adopted for experiments discussed in sections below. More specifically, experiments are focused onto the detection of *B. atrophaeus* spores, through its characteristic molecule CaDPA (calcium dipicolinate) and corresponding strong Raman vibrations at 1018, 1395, and 1445 cm^{-1} [25,26]. To this regard, Fig. 2(b) shows the dependence of $\left|S_{12}(\Omega)\right|^2$ on the parameter β for the Raman shifts of 1018, 1395, and 1445 cm^{-1}, and, for the sake of comparison, of 1290 cm^{-1}, which is the center frequency of the excitation profile. As it can be seen, for $\beta \ll 1$ ($\Delta\omega_2 \ll \Delta\omega_1$), the excitation is far from being optimized, due to the time gating effect of the pump pulse onto the Stokes, which prevents efficient use of the Stokes pulse energy content. Increasing the β parameter results in a monotonic growth of the spectral response at all frequencies, till reaching the condition $\beta = 1$, which corresponds to maximized response at the center frequency of 1290 cm^{-1}. Interestingly, for β>1, the excitation at sufficiently large detunings with respect to the center progressively improves at the expense of the frequencies around the center; therefore, depending on the characteristic frequencies of the target of interest, it may be useful to operate the system with β>1 to improve the overall

Optics EXPRESS

visibility of the Raman spectral response. In the case of *B. atrophaeus* spores discussed below, the condition $\beta \cong 1.35$ allows for an improved response at 1018 and 1445 cm^{-1}, while providing only a minor attenuation at 1395 cm^{-1}.

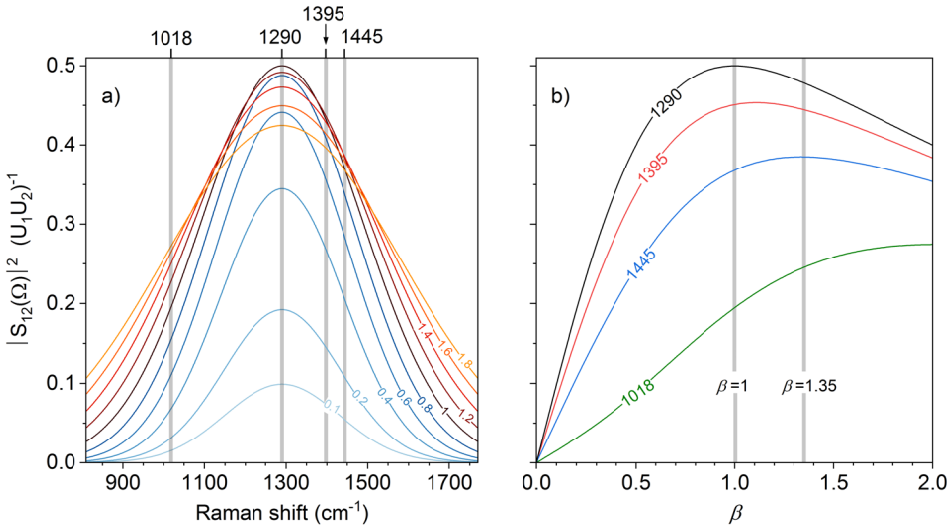

Fig. 2. a) Absolute square of the excitation profile $|S_{12}(\Omega)|^2$ as a function of the Raman shift for several values of the β parameter from 0.1 to 1.8, assuming $\Delta\omega_1/2\pi$=340 cm^{-1} and $\Omega_0/2\pi$=1290 cm^{-1}. b) $|S_{12}(\Omega)|^2$ as a function of β for the Raman shift of 1018, 1290 (center frequency), 1395, and 1445 cm^{-1}.

3. Experimental setup

The layout of the experimental setup used for hybrid-CARS measurements is shown in Fig. 3. It starts with an amplified Yb:KGW laser (Pharos, Light Conversion), generating ~250-μJ, 250-fs pulses at 1025 nm, with ~6-nm (59-cm^{-1}) full width at half maximum (FWHM) bandwidth, and 1-kHz repetition rate. The output beam is split by a partial reflector into a transmitted and reflected beam with an energy per pulse of 13 and 240 μJ, respectively. The transmitted beam is coupled into a hypocycloid core-contour Kagome HCPCF with a length of 60 cm and inner core diameter of 57 μm. The measured $1/e^2$ mode field diameter is 39 μm. The combination of a half-wave plate and a thin film polarizer allows for fine tuning of the pulse energy coupled into the HCPCF and hence, of the spectral broadening resulting from it. The HCPCF is placed within a stainless steel tube with pressure chambers and anti-reflection (AR) coated windows on both sides; the chambers are filled with Krypton at a pressure of 13 bar, providing nonlinear broadening within the pure self-phase-modulation regime. The bandwidth of the Stokes pulses generated by the HCPCF can be changed by adjusting the orientation of two tunable short- and long-wave pass (SP and LP) filters (Semrock Versachrome, cutoffs tunable from 975 to 1115 nm) with respect to the beam; additionally, a variable neutral density filter is used to keep constant the energy of the Stokes pulse incident onto the sample. Pulses at the output of the HCPCF are passed through a compressor based on six bounces on chirped mirrors which introduces an overall group delay dispersion (GDD) of 6×-550 fs^2 in the range of wavelength from 900 to 1150 nm. The beam reflected from the partial reflector, with an energy per pulse of 240 μJ, is sent to a 3-stage optical parametric amplifier (OPA) based on white-light continuum generation in a YAG plate and non-collinear parametric amplification by beta-barium-borate (BBO) crystals. The OPAs are pumped by the second harmonic (SH) of the fundamental at 1025nm. Detailed

Optics EXPRESS

description and performance of the three-stage OPA can be found elsewhere [18]. However, differently from the prism compressor utilized before, the pulses at the output of the OPA are now compressed using a couple of chirped mirrors (complementary GDD design) providing an overall GDD of 20×-150 fs^2.

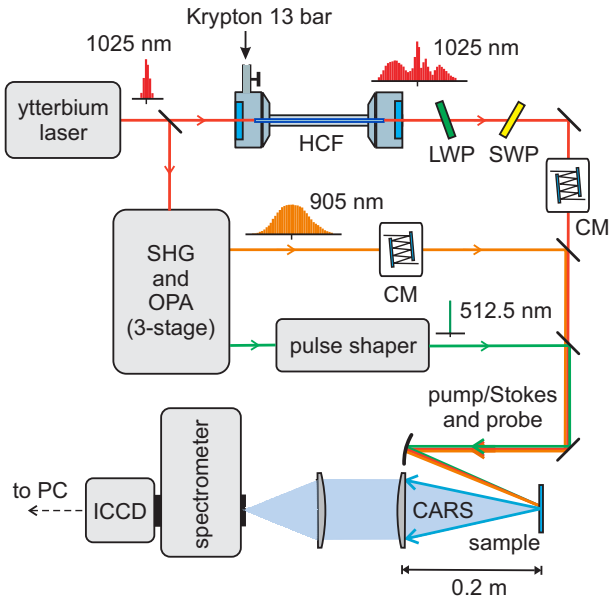

Fig. 3. Layout of the hollow-core fiber compressor and OPA source for CARS spectroscopy. HCF: hollow-core fiber; CM: chirped mirror; LWP: Long-wave pass filter; SWP: Short-wave pass filter; ICCD: Intensified CCD camera.

The compressed laser pulses generated by the OPA and HCPCF have been characterized in the time and frequency domain by SH frequency resolved optical gating (SH-FROG) analysis. Figures 4(a),(c) and (b),(d) show the experimental and retrieved SH-FROG maps for the compressed pulses generated by the OPA and HCPCF, respectively; Figs. 4(e),(g) and (f),(h) show the retrieved spectral and temporal intensity and phase profiles, along with the corresponding experimental spectra. The spectral phase in Fig. 4(e) shows a residual negative quadratic phase corresponding to a GDD of −130 fs^2. This is consistent with the minimum step of GDD compensation provided by the chirped mirror compressor corresponding to 2×-150 fs^2 (complementary GDD design requires one bounce on each matched mirror), as we found longer pulse durations for both 18 or 22 bounces, i.e. different from the optimal 20 bounces, meaning that larger amounts of GDD are left uncompensated in those cases. Besides this, the measured pulsewidth of 50 fs is very close to the transform-limited value (44 fs), meaning that overall the spectral phase is well compensated, and the residual chirp has only a marginal effect on pulse duration.

By the end of the HCPCF-based non-linear broadening and OPAs, the laser system produces three separate beams used as the pump, Stokes and probe for CARS interaction. The first beam is the Stokes, with an energy per pulse of 7 μJ at 1025 nm, a FWHM bandwidth of 47 nm (445 cm^{-1}), and a duration of 48 fs; the second beam is the pump, with an energy per pulse of 15 μJ at 905 nm, a FWHM band of 27 nm (330 cm^{-1}) and a duration of 50 fs; finally, the third beam is the probe, with an energy per pulse of 9 μJ at 512.5 nm, a FWHM bandwidth of ~0.2 nm (8 cm^{-1}) and a duration of ~4.2 ps, obtained from the SH left unconverted after OPA interaction and spectrally narrowed in a zero dispersion pulse shaper. The pulse shaper is configured in a standard 4f design using two reflection gratings and two thin lenses; a variable-width slit placed

Optics EXPRESS

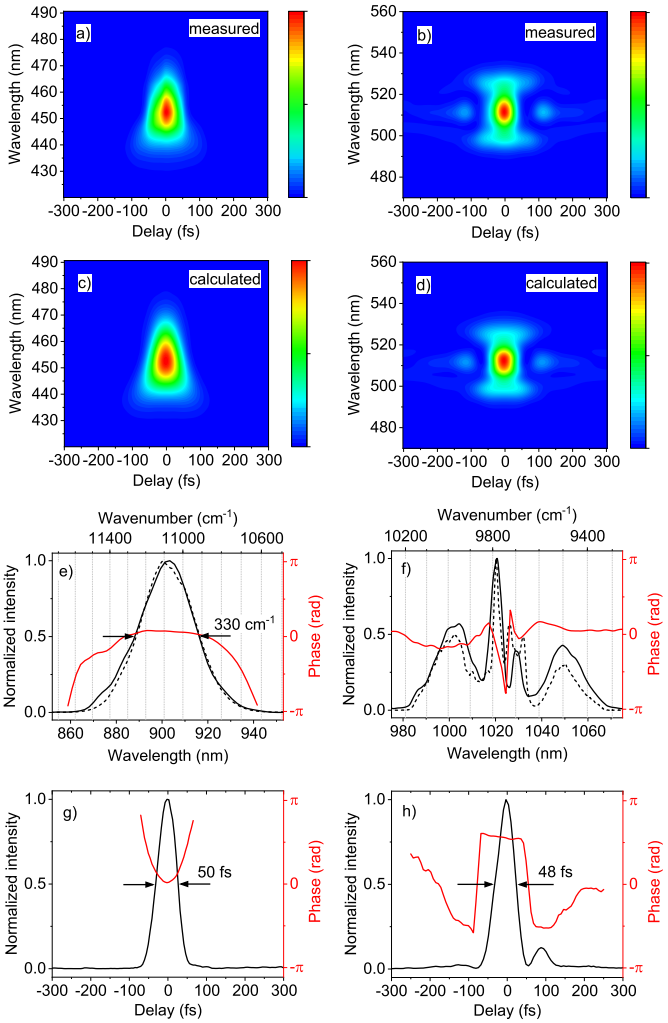

Fig. 4. Characterization of laser pulses at the output of the OPA (left) and HCPCF (right) after dispersion compensation by chirped mirror pairs. a,b) Measured SHG-FROG traces, and c,d) reconstructed FROG traces with errors below 0.01 on 512 × 512 grids. e,f) Reconstructed (solid) and measured (dotted) spectral intensity and phase. g,h) Reconstructed temporal intensity and phase. The compressed pulse durations are suitably matched.

Optics EXPRESS

in the focal plane of the pulse shaper allows for tuning of the transmitted probe pulse bandwidth. In addition, the slit provides a rectangular-like transmission in the spectral domain, corresponding to a sinc-squared probe pulse intensity profile in the time domain given by $\Delta\nu_3\ \mathrm{sinc}^2(\Delta\nu_3 t)$, with $\Delta\nu_3$ the bandwidth of the probe pulse as set by the variable-width slit. It should be noted that our previous design of the pulse shaper [18,22] was based on a 0.5-mm thickness fused silica transmission grating with 1274 lines/mm and a useful area of 4×4 mm^2, while the design used for the experiments presented here is based on silver-coated reflection gratings with 1200 lines/mm an area of 25×25 mm^2. While the numbers of lines/mm are substantially similar, the dimensions of the grating area are five times larger in the present design, which allowed us for increasing the diameter of the beam incident onto the grating, ultimately leading to an improvement of resolution in the pulse shaper by a factor of 5.

The three beams are multiplexed in a collinear arrangement and focused by a spherical mirror (focal length of 300 mm) onto the target sample, placed at a distance of 30 cm. The $1/e^2$ diameter of the three laser beams on the target is ~40 μm. The back-scattered CARS signal is collected by a 2-inches lens with 200-mm focal length and focused onto the entrance slit of a spectrometer equipped with an intensified CCD camera (gating time of 2 ns).

4. Experiments

Experiments have been conducted to confirm the trends obtained from the theoretical model presented in Sec.2. This requires a measurement of the excitation profile $|S_{12}|^2$ for increasing values of the β parameter, starting from $\beta \ll 1$ up to $\beta > 1$. To this purpose, we made a pellet of sodium chloride (NaCl) and measured the corresponding CARS spectra for several bandwidths of the Stokes pulse, while keeping its energy constant; as the resonant response of NaCl from 750 to 2800 cm^{-1}, which is the range of interest to our application, is extremely weak or even absent, the approximation $\chi_R^{(3)} \cong 0$ holds in this case, and a measurement of I_{CARS} represents a close estimation of $|S_{12}|^2$, up to a scaling factor. The bandwidth of the Stokes pulse has been changed from 59 to 446 cm^{-1}, which corresponds to a β parameter going from 0.18 to 1.35, taking into account the pump pulse bandwidth of 330 cm^{-1}; Fig. 5(a)-f shows the Stokes pulse spectra normalized to the maximum intensity, for the purpose of better visualization. The Stokes pulse durations have been measured using the SH-FROG analysis and found in close agreement with the Fourier transform limit obtained by taking into account the specified β parameters and corresponding bandwidths. Figure 5(g)-n shows the corresponding spectrograms of NaCl; as expected, the intensity of the spectrograms grows while the β parameter is changed from 0.18 to 1.35, even though all pulse energies, particularly that of the Stokes, are kept constant. It is also worth noting the presence of two nodes at ±2.1 ps and two sidelobes corresponding to the sinc-shaped probe pulse profile. The vertical cross-sections at 0-ps probe delay are reported in Fig. 6(a); up to a common scaling factor, they represent the required excitation profiles $|S_{12}|^2$ for six different values of β from 0.18 to 1.35. Again, the amplitude of the excitation profiles increases with the β parameter; in addition, the FWHM bandwidth grows from 336 to 555 cm^{-1}. The experimental $|S_{12}|^2$ exhibit bell-shaped spectral profiles similar to Gaussians, even though the spectra of the Stokes pulse are quite structured; this is due to the cross-correlation between the pump and Stokes, which smooths out the spectral features of the Stokes. Indirectly, this also validates the simplifying assumptions made within our model that both the pump and Stokes pulses have Gaussian spectra. Figure 6(b) shows the amplitude of the excitation profiles at increasing β parameter values corresponding to the three main resonances of CaDPA at 1018, 1395, and 1445 cm^{-1}. The experimental data have been fitted with the profile expressed by Eq. (15) using β as the independent variable; overall, the agreement is good, though slight deviations from the model are present, mainly ascribed to variation of the central frequency

Optics EXPRESS

of the excitation profile while tuning the cutoff frequencies of the SP and LP filters utilized to change the β parameter.

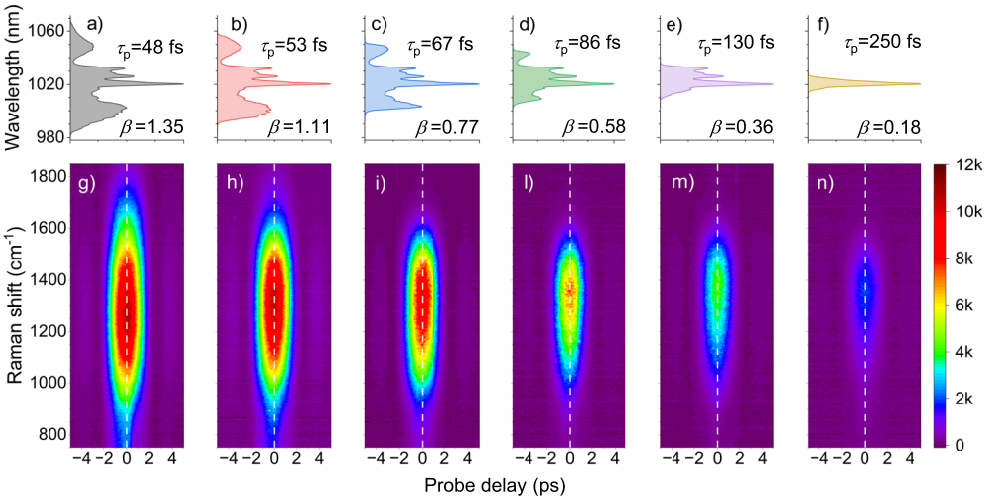

Fig. 5. a-f) The spectra of the Stokes pulses used to reproduce different β parameters; in all cases the pulse energy is of 1 μJ. The measured Stokes pulse durations are shown. g-f) The CARS spectrograms of NaCl as measured for different durations (β parameters) of the Stokes pulses. The white dotted lines indicate the cross sections shown in Fig. 6. All pulse energies of the pump, Stokes, and probe have been set 0.1 μJ, and CCD integration time is 1 s;

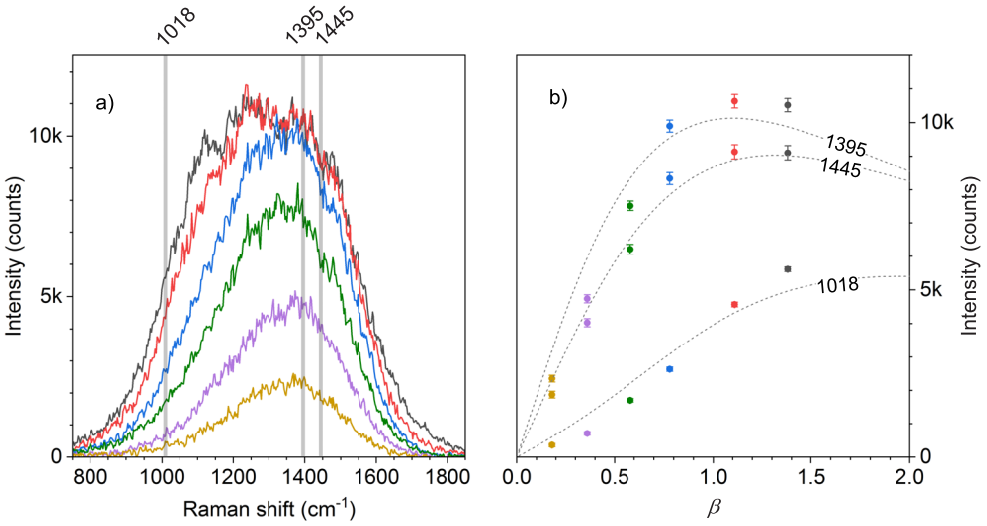

Fig. 6. a) The cross sections of the CARS spectrograms shown in Fig. 5 for different β parameters and a probe pulse delay of 0 ps. The gray lines highlight the three spectral components at 1018, 1395, and 1445 cm^{-1}, characteristics of CaDPA, used for bacterial spores detection. b) The intensity of the CARS signal for different β parameters at 1018, 1395, and 1445 cm^{-1}. Dotted gray lines represent best fits of Eq. (6) to experimental data. Error bar represents the standard deviation ($\pm\sigma$) of noise within a small spectral interval of 50 cm^{-1} around the selected frequencies.

Optics EXPRESS

Basing on the results shown before, we moved to a more challenging sample of *B. atrophaeus* spores, to show how detection is improved by tailoring the Stokes pulse bandwidth close to the condition corresponding to β=1.35. The spore sample is deposited on a fused silica plate and placed at a distance of 0.2 m from the collection lens with 20-cm focal length; the integration time of the CCD camera is set to 1 ms, therefore a CARS spectrum obtained under this condition is contributed by a single pump, Stokes, and probe laser pulse. First, the spectrogram of *B. atrophaeus* spores has been measured for probe delays from 0 to 3.2 ps, and by averaging over five consecutive laser pulses. More specifically, in this case single laser pulses are fired on-demand through manual control while the camera is operated in the "accumulate" mode (5 accumulated spectra, acquisition is kept in standby until a trigger from the laser starts an acquisition with an integration time of 1 ms). The result is shown in Fig. 7(a), where apparent streaklike horizontal lines are the Raman signature of the CaDPA contained within the spore cores. Ideally, hybrid-CARS spectroscopy allows for isolating the resonant contribution of a molecular target with respect to the NRB by working at a probe delay corresponding to the node of the sinc-shaped probe, that is 2.1 ps in our system. However, the Raman response of spores is extremely weak, due to the small amount of contributing sample, and its exponential decays are almost extinguished at probe delays of 2.1 ps. On the other hand, it should be noted that the interference with the NRB obtained before the node of the sinc probe, usually detrimental due to the distortions induced on lineshapes, provides also an heterodyne amplification resulting in an overall gain of signal strength which could help with detection. This is the case of the bacterial spore sample analyzed in Fig. 7(a), where the best compromise between the resonant signal and NRB is observed at a probe delay of 1.2 ps; the corresponding vertical cross-section of the spectrogram is shown in Fig. 7(c). Here, three Raman lines at 1018, 1395, and 1445 cm^{-1} are clearly visible; this triplet provides a unique combination of frequencies which can be confidently ascribed to CaDPA [25,26]. In particular, the lines at 1018 and 1445 cm^{-1} correspond to symmetric "breathing" and C-C stretching modes of the pyridine ring, whereas the line at 1395 cm^{-1} is related to C-O stretch in the carboxyl group of CaDPA molecule. The interference with the NR background could be in principle a limit for quantitative measurements, however, deep learning as well as other computer-based techniques can help recovering the pure resonant response from the data distorted by interference with the NRB [27]. The horizontal cross section of the spectrogram at 1320 cm^{-1} is shown in Fig. 7(b); here, the pump and Stokes pulses are basically sampling the probe pulse in time, due to their much shorter durations, therefore providing a measurement of its intensity profile, close to a sinc-squared as expected.

We now turn to investigating the performance of the system for detection of bacterial spores using a single laser shot. Figure 8(a) shows the hybrid-CARS spectrum of *B. atrophaeus* spores corresponding to β parameters of 0.18 and 1.35, that is a narrowband Stokes, similar to that used with our previous setup [22], and a broadband Stokes, optimized for CaDPA detection according to the rationale discussed in Sec.2, respectively. The resonant contribution is retrieved by fitting the NRB (asymmetric least square fit, ALS [28]) and subtracting the fit from the raw spectra; the result is shown in Fig. 8(b), along with the reference SR spectrum of CaDPA. The three main Raman lines at 1018, 1395, and 1445 cm^{-1} of CaDPA within the core of spores are clearly resolved in the case of β=1.35, which is very notable, considering that a single pump, Stokes, and probe pulse is used to illuminate the sample and hence is contributing to the measurement. The SNR observed in this case, defined as the ratio between the amplitude of the most intense peak at 1445 cm^{-1} and the rms amplitude of noise from 1250 to 1350 cm^{-1}, is around 12. In the case of β=0.18 the doublet of lines at 1395 and 1445 cm^{-1} is barely visible, with a SNR of around 2.5, whereas the line at 1018 cm^{-1} is not visible at all. The counts observed on the peak at 1445 cm^{-1} are ~3900 and ~470 with β parameter of 1.35 and 0.18, respectively; the ratio between the counts is then 3900/470≅8.2, which is slightly better then the ratio of ~4.8 predicted by the model, ascribed to a more pronounced heterodyning effect by the stronger NRB

Optics EXPRESS

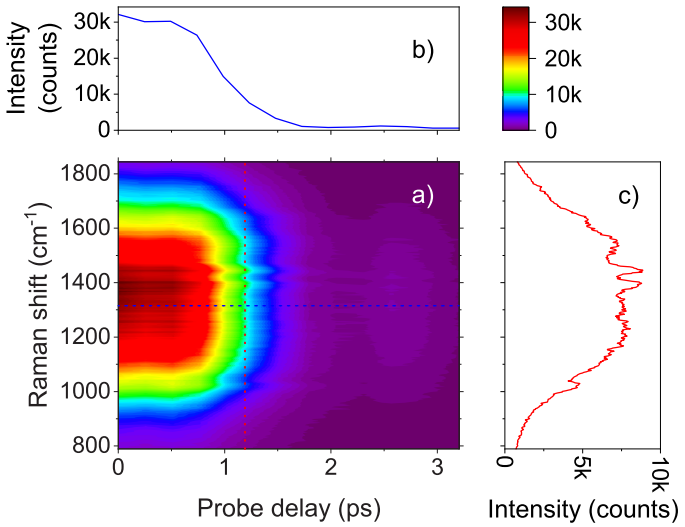

Fig. 7. a) CARS spectrogram of *B. atrophaeus* spores as observed for a β parameter of 1.35. Each vertical section (spectrum) has been measured by averaging over 5 consecutive spectra at a constant delay. b) A sinc-shaped horizontal cross section at 1320 cm^{-1}. c) A vertical cross section at 1.2 ps with near optimal SNR. Pulse energy of the pump, Stokes, and probe have been set to 3, 3, 1 μJ, respectively; CCD integration time is 1 ms; the sample is at a distance of 20 cm from the collection lens.

observed in the case β=1.35. The pulse energies of the pump, Stokes, and probe have been set to 3, 3, and 1 μJ, respectively, corresponding to a fluence of ~0.5 J/cm^2 for the femtosecond pump and Stokes pulses. This combination has been found empirically to keep the effects of induced photodamage on our sample of *B. atrophaeus* spores at sufficiently low levels while optimizing the CARS signal; more specifically, under this experimental condition we observed a typical degradation (reduction) of the CARS signal to ~10% of its original intensity after a sequence of ~20 laser pulses due to cumulative photodamage induced on the sample. This is consistent with the observation of induced photodamage reported in [21] for *B. subtilis* spores and, more generally, with the damage fluence threshold of ~1 J/cm^2 typically observed in biological tissues [29].

The amount of CaDPA in the spores contributing to the CARS signal can also be estimated, which is an indication of the sensitivity of the system for bacterial spore detection. On average, a single spore of *B. atrophaeus* contains 49 fg of CaDPA salt in the core, because the mass of a dry spore is 328 fg [30], and the relative mass of CaDPA is generally assumed to be around 15%. As the mean volume of *B. atrophaeus* spores is of 0.27 μm^3 [30], we assumed an effective volume of 1 μm^3 for the close packed spores of our deposited sample. Basing on the the laser beam diameter of 40 μm on the sample, and assuming an effective laser penetration depth of 10 μm [31], the number of spores contained within the volume probed by the laser beam (2.5×10^3 μm^3) is estimated to be 2.5×10^3, corresponding to ~0.1 ng of CaDPA at a SNR of 12 using a single laser shot.

Optics EXPRESS

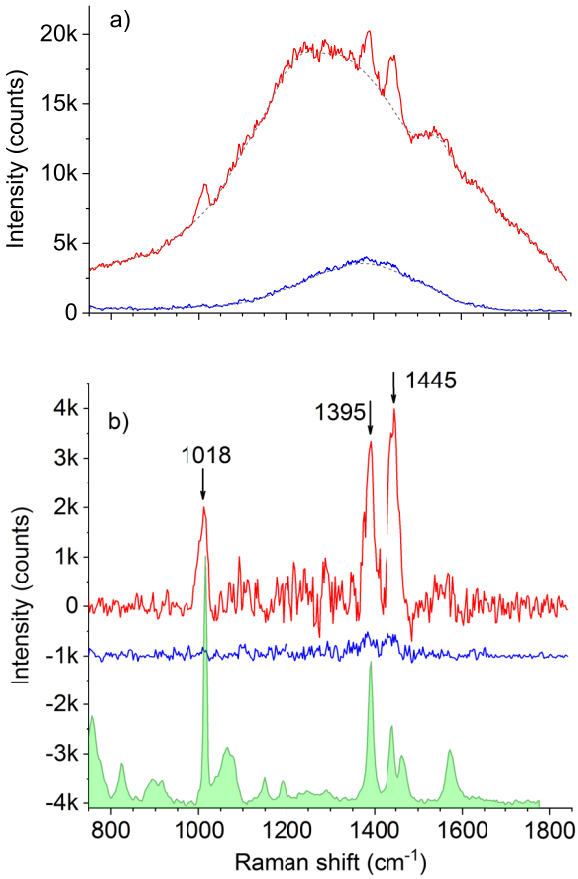

Fig. 8. a) Single-shot CARS spectra of *B. atrophaeus* spores as measured for a β parameter of 0.18 (blue line) or 1.35 (red line) along with corresponding baselines (dashed gray lines) obtained through ALS fit (threshold 0.18, 3-point window, 10 iterations). b) The resonant CARS signature of *B. atrophaeus* spores after baseline removal; note that for β=0.18, the strong doublet at 1395 and 1445 cm^{-1} is only barely visible whereas the line at 1018 cm^{-1} is not detected at all. The reference SR spectrum of CaDPA is also shown (green line). Pulse energy of the pump, Stokes, and probe have been set to 3, 3, 2 μJ, respectively; CCD integration time is 1 ms; the sample is at a distance of 20 cm from the collection lens.

Optics EXPRESS

5. Conclusion

We have extended our previous hybrid-CARS setup, based on a high-energy femtosecond Yb-laser and an OPA, by the adoption of a HCPCF filled with krypton, with the purpose of compressing the Stokes pulse, which had a duration much longer than the pump. By doing this, we have been able to avoid the time gating effect introduced by pump onto the Stokes, which prevented a full exploitation of the available pulse energies. We have adapted the theory of hybrid-CARS to model this effect and predict the potential improvement of line intensities observed in a typical spectral measurement, by matching the durations of the two preparation pulses. We confirmed the trends predicted by the model with experimental measurements. Finally, we have applied our extended setup to detection of bacterial spores deposited on a surface at a distance of 0.2 m from the laser system. We have detected 2.5×10^3 *B. atrophaeus* spores, corresponding to ~1 ng of CaDPA, which is the Raman marker characteristic of spores, with a SNR of 12 using a single laser shot. The observed SNR, bandwidth, and overall spectral quality, are superior to any previous hybrid-CARS setup based on Ti:sapphire systems and are promising for applications to the detection of hazardous bioagents.

Funding. Defence Science and Technology Laboratory (DSTLX-1000131285, DSTLX-1000132350).

Disclosures. The authors declare no conflicts of interest.

Data availability. Data underlying the results presented in this paper are not publicly available at this time but may be obtained from the authors upon reasonable request.

References

1. C. L. Evans and X. S. Xie, "Coherent anti-stokes raman scattering microscopy: Chemical imaging for biology and medicine," Annu. Rev. Anal. Chem. **1**(1), 883–909 (2008). PMID: 20636101.
2. D. Polli, V. Kumar, C. M. Valensise, M. Marangoni, and G. Cerullo, "Broadband coherent raman scattering microscopy," Laser Photonics Rev. **12**(9), 1800020 (2018).
3. C. L. Evans, E. O. Potma, and X. S. Xie, "Coherent anti-stokes raman scattering spectral interferometry: determination of the real and imaginary components of nonlinear susceptibility χ^3 for vibrational microscopy," Opt. Lett. **29**(24), 2923–2925 (2004).
4. E. O. Potma, C. L. Evans, and X. S. Xie, "Heterodyne coherent anti-stokes raman scattering (CARS) imaging," Opt. Lett. **31**(2), 241–243 (2006).
5. D. Pestov, G. O. Ariunbold, X. Wang, R. K. Murawski, V. A. Sautenkov, A. V. Sokolov, and M. O. Scully, "Coherent versus incoherent raman scattering: molecular coherence excitation and measurement," Opt. Lett. **32**(12), 1725–1727 (2007).
6. T. W. Kee, H. Zhao, and M. T. Cicerone, "One-laser interferometric broadband coherent anti-stokes raman scattering," Opt. Express **14**(8), 3631–3640 (2006).
7. C. H. Camp Jr, Y. J. Lee, J. M. Heddleston, C. M. Hartshorn, A. R. H. Walker, J. N. Rich, J. D. Lathia, and M. T. Cicerone, "High-speed coherent raman fingerprint imaging of biological tissues," Nat. Photonics **8**(8), 627–634 (2014).
8. R. Selm, M. Winterhalder, A. Zumbusch, G. Krauss, T. Hanke, A. Sell, and A. Leitenstorfer, "Ultrabroadband background-free coherent anti-stokes raman scattering microscopy based on a compact er:fiber laser system," Opt. Lett. **35**(19), 3282–3284 (2010).
9. D. Oron, N. Dudovich, and Y. Silberberg, "Femtosecond phase-and-polarization control for background-free coherent anti-stokes raman spectroscopy," Phys. Rev. Lett. **90**(21), 213902 (2003).
10. N. Dudovich, D. Oron, and Y. Silberberg, "Single-pulse coherent anti-stokes raman spectroscopy in the fingerprint spectral region," J. Chem. Phys. **118**(20), 9208–9215 (2003).
11. H. U. Stauffer, J. D. Miller, S. Roy, J. R. Gord, and T. R. Meyer, "Communication: Hybrid femtosecond/picosecond rotational coherent anti-stokes raman scattering thermometry using a narrowband time-asymmetric probe pulse," J. Chem. Phys. **136**(11), 111101 (2012).
12. R. Santagata, M. Scherman, M. Toubeix, M. Nafa, B. Tretout, and A. Bresson, "Ultrafast background-free ro-vibrational fs/ps-cars thermometry using an yb:yag crystal-fiber amplified probe," Opt. Express **27**(23), 32924–32937 (2019).
13. M. T. Bremer, P. J. Wrzesinski, N. Butcher, V. V. Lozovoy, and M. Dantus, "Highly selective standoff detection and imaging of trace chemicals in a complex background using single-beam coherent anti-stokes raman scattering," Appl. Phys. Lett. **99**(10), 101109 (2011).
14. M. T. Bremer and M. Dantus, "Standoff explosives trace detection and imaging by selective stimulated raman scattering," Appl. Phys. Lett. **103**(6), 061119 (2013).

Optics EXPRESS

15. H. Li, D. A. Harris, B. Xu, P. J. Wrzesinski, V. V. Lozovoy, and M. Dantus, "Standoff and arms-length detection of chemicals with single-beam coherent anti-stokes raman scattering," Appl. Opt. **48**(4), B17–B22 (2009).
16. G. Rasskazov, A. Ryabtsev, and M. Dantus, "Eye-safe near-infrared trace explosives detection and imaging," Opt. Express **25**(6), 5832–5840 (2017).
17. O. Katz, A. Natan, Y. Silberberg, and S. Rosenwaks, "Standoff detection of trace amounts of solids by nonlinear raman spectroscopy using shaped femtosecond pulses," Appl. Phys. Lett. **92**(17), 171116 (2008).
18. D. Gatti, M. Lamperti, A. Zilli, F. Canella, G. Cerullo, G. Galzerano, P. Laporta, and N. Coluccelli, "Standoff cars spectroscopy and imaging using an ytterbium-based laser system," Opt. Express **30**(9), 15376–15387 (2022).
19. H. U. Stauffer, J. D. Miller, M. N. Slipchenko, T. R. Meyer, B. D. Prince, S. Roy, and J. R. Gord, "Time- and frequency-dependent model of time-resolved coherent anti-stokes raman scattering (cars) with a picosecond-duration probe pulse," J. Chem. Phys. **140**(2), 024316 (2014).
20. D. Pestov, R. K. Murawski, G. O. Ariunbold, X. Wang, M. Zhi, A. V. Sokolov, V. A. Sautenkov, Y. V. Rostovtsev, A. Dogariu, Y. Huang, and M. O. Scully, "Optimizing the laser-pulse configuration for coherent raman spectroscopy," Science **316**(5822), 265–268 (2007).
21. D. Pestov, X. Wang, G. O. Ariunbold, R. K. Murawski, V. A. Sautenkov, A. Dogariu, A. V. Sokolov, and M. O. Scully, "Single-shot detection of bacterial endospores via coherent raman spectroscopy," Proc. Natl. Acad. Sci. **105**(2), 422–427 (2008).
22. N. Coluccelli, G. Galzerano, P. Laporta, K. Curtis, C. L. Lonsdale, D. Padgen, C. R. Howle, and G. Cerullo, "Standoff detection of bacterial spores by field deployable coherent raman spectroscopy," Sci. Rep. **13**(1), 2634 (2023).
23. E. Vicentini, A. Gambetta, G. Galzerano, P. Laporta, K. Curtis, K. McEwan, C. R. Howle, and N. Coluccelli, "Fiber laser system for standoff coherent raman spectroscopy," Opt. Lett. **45**(21), 5925–5928 (2020).
24. N. Coluccelli, P. Laporta, G. Cerullo, K. Curtis, K. McEwan, and C. R. Howle, "A compact fiber-laser-based system for detection of biological agents via coherent Raman spectroscopy," in *Chemical, Biological, Radiological, Nuclear, and Explosives (CBRNE) Sensing XXII*, vol. 11749 J. A. Guicheteau and C. R. Howle, eds., International Society for Optics and Photonics (SPIE, 2021), pp. 92–97.
25. L. Kong, P. Setlow, and Y.-q. Li, "Analysis of the raman spectra of Ca^{2+}-dipicolinic acid alone and in the bacterial spore core in both aqueous and dehydrated environments," Analyst **137**(16), 3683–3689 (2012).
26. Y. Huang, A. Dogariu, Y. Avitzour, R. K. Murawski, D. Pestov, M. Zhi, A. V. Sokolov, and M. O. Scully, "Discrimination of dipicolinic acid and its interferents by femtosecond coherent raman spectroscopy," J. Appl. Phys. **100**(12), 124912 (2006).
27. C. M. Valensise, A. Giuseppi, F. Vernuccio, A. De la Cadena, G. Cerullo, and D. Polli, "Removing non-resonant background from CARS spectra via deep learning," APL Photonics **5**(6), 061305 (2020).
28. P. H. C. Eilers, "A perfect smoother," Anal. Chem. **75**(14), 3631–3636 (2003). PMID: 14570219.
29. M. H. Niemz, *Laser-Tissue Interactions* (Springer, 2007).
30. M. Carrera, R. O. Zandomeni, and J.-L. Sagripanti, "Wet and dry density of bacillus anthracis and other bacillus species," J. Appl. Microbiol. **105**(1), 68–77 (2008).
31. Y. Huang, A. Soroka, K. Cohen, and A. Dogariu, "Backscattered coherent anti-stokes raman scattering for at range detection of dipicolinic acid and four-wave mixing multiple scattering," J. Mod. Opt. **54**(16-17), 2473–2480 (2007).